*Manuscript
Click here to view linked References

EVALUATION OF DIRECT LIGHT PROCESSING FOR THE FABRICATION OF BIOACTIVE CERAMIC SCAFFOLDS: EFFECT OF PORE/STRUT SIZE ON MANUFACTURABILITY AND MECHANICAL PERFORMANCE

Claudia Paredes[1], Francisco J. Martínez-Vázquez[1,*], Hamada Elsayed[2,3], Paolo Colombo[2,4], Antonia Pajares[1] and Pedro Miranda[1]

[1] Department of Mechanical, Energy and Materials Engineering, University of Extremadura, Avda. de Elvas s/n., 06006 Badajoz, Spain

[2] Department of Industrial Engineering, University of Padova, Italy

[3] Ceramics Department, National Research Centre, 12622 Dokki, Cairo, Egypt

[4] Department of Materials Science and Engineering, The Pennsylvania State University, University Park, PA 16802, USA

* Corresponding author: Francisco J. Martínez-Vázquez E-Mail: fjmartinezv@unex.es; Tel: +34-924-289-300; Fax: +34-924-289-601.

Abstract

Bioactive ceramic scaffolds for bone regeneration consisting of a three-dimensional mesh of interpenetrating struts with square section were fabricated via Digital Light Processing (DLP). The ability of the technique to manufacture 3D porous structures from β-tricalcium phosphate (β-TCP) powders with different dimensions of struts and pores was evaluated, identifying the possibilities and limitations of the manufacturing process. Small pore sizes were found to seriously complicate the elimination of excess slurry from the scaffold's innermost pores. The effect of the strut/pore size on the mechanical performance of the scaffolds under compressive stresses was also evaluated, but no significant influence was found. Under compressive stresses, the structures resulted weaker when tested perpendicularly to the printing plane due to interlayer shear failure. Interlayer superficial grooves are proposed as potential failure-controlling defects, which could also explain the lack of a Weibull size effect on the mechanical strength of the fabricated DLP scaffolds.

Keywords: Scaffolds; Ceramic; Mechanical properties; Digital Light Processing

1. Introduction

As the world population continues its progressive ageing, the need of restorative surgeries to reestablish the normal functionality of damaged bone tissue has increased [1–3]. Due to existing limitations of currently available techniques for the substitutive repair of large bone lesions with artificial implants, the development of biodegradable bone scaffolds capable of inducing bone regeneration is presently a recurring research subject. Among these studies, the use of different Additive Manufacturing (AM) techniques to fabricate these bioactive porous substrates has received increasing attention due to their extraordinary versatility and the geometrical control they provide both at the microstructural and macroscopic levels [4–6].

Biodegradable scaffolds must facilitate the interaction with the surrounding tissue, ensuring the migration of bone cells to their interior, in order to actively induce bone regeneration before their complete degradation [4]. This requires the use of materials with adequate mechanical performance and osteoconductive properties. Bioactive ceramics (such as calcium phosphates or calcium sulfate and bioactive 45S5 and 13-93 glasses, etc.) are often an ideal choice, due to their capacity to interact with the surrounding tissue and their similarities in composition to the inorganic phase of bone [1,4,7]. Among the calcium phosphates, β-tricalcium phosphate (β-TCP) is a preferred choice since it can actively induce bone ingrowth and has a most adequate degradation rate [4,8].

The downside of all these bioceramic materials is their low mechanical performance in terms of brittleness and strength [9]. The latter is especially compromised when fabricating scaffolds with high porosity levels [10]. Digital Light Processing (DLP), among other AM techniques, enables the fabrication of complex structures with very high resolutions and

shorter printing times [11,12]. This not only allows the scaffolds fabricated by DLP to perfectly fit the patient's lesion, but also provides a singular level of control on the size and distribution of their interconnected pores leading to higher load bearing capacities, as demonstrated in scaffolds fabricated by different AM techniques [6,13–15].

DLP as its sister AM technique, stereolithography (SLA), is based on the crosslinking of a photosensitive liquid resin selectively induced by a source of light with the appropriate wavelength in the UV or visible range [12,16]. While SLA uses a UV-laser to cure the resin point-by-point, DLP systems use a UV-visible light projector to cure a whole layer of the part by sequentially projecting onto the resin the images of the different cross sections that make up the structure [12,16]. Printed parts stay attached to the printing base, which can move vertically towards and away from the resin vat, to let fresh resin flow beneath the part after each layer is printed. Typical layer thickness ranges from 20 to 100 microns, depending on the required minimum feature size and macroscopic architecture of the part.

Acrylic resins are commonly used due to their capacity to rapidly polymerize at room temperature [17]. These resins are generally composed of multifunctional monomers with typically (meth)acrylate or epoxy groups, a photoinitiator and a light absorber, whose relation with the UV emission spectrum of the equipment must be optimized [17]. The photo-absorber helps controlling the penetration depth and the scattering of the light, which in turn determine the manufacturing resolution in the printing direction (Z-direction) and in-plane (XY-directions), respectively.

The fabrication of ceramic structures by this technique is possible by adding a ceramic filler to the resin, thus creating a slurry whose organic component is susceptible to polymerization when the light irradiates the suspension, trapping the ceramic particles in

place after the exposure [12,16]. The suspension viscosity must remain as low as possible—a maximum value of 3 Pa·s is typically quoted, although higher values are possible depending on the DLP printer configuration— to ensure its free flow during the printing process [12,18], which limits the solid loading in the slurry. The low solid content can potentially lead to cracking problems either when eliminating the organics present in the printed part or during subsequent sintering, where it can also reduce densification, and, thus, limits the mechanical performance of the final part. The refractive index of the ceramic phase plays likewise a crucial role in the printing process since the inorganic particles can interfere with the irradiation of the polymer by producing light scattering, which decreases the resolution in the XY plane and the penetration depth of the radiation in the Z direction. Therefore, optimal printing results are obtained when the refractive index of the resin and the ceramic powder are similar [12,18,19]. In addition to affecting the printing process, the concentration of the ceramic also determines the volume change occurring in the structures when they are subjected to a subsequent high temperature sintering treatment, which is necessary to impart the desired properties to the final parts. Since the shrinkage will be lower the higher the powder concentration is, it is necessary to reach a balance between the two conflicting requirements [12].

Despite the difficulties, the fabrication of bone implants by DLP using ceramic fillers in photocurable resins is being pursued by many authors due to the great potential of this manufacturing technique. Both bioinert ceramics, such as alumina and zirconia, [16,20], as well as bioactive compositions such as hydroxyapatite or calcium phosphates [16,21–23] and especially bioactive glasses [24–26] have been successfully fabricated by these vat photopolymerization techniques (SLA/DLP). However, to date, there are no studies in the

literature dedicated to systematically evaluating the effects of pore and strut size on the manufacturability and mechanical performance of bioactive ceramics scaffolds fabricated by DLP

Thus, the objective of this study was the investigation of the effect of feature (pore and strut) size on the fabrication and properties of β-tricalcium phosphate (β-TCP) scaffolds for bone regeneration produced by DLP. In particular, the limitations on feature size imposed by the printing process when using a ceramic/resin suspension were evaluated, and the effect of pore and strut size on the mechanical properties of scaffolds with the same pre-designed macroporosity was analyzed.

2. Materials and methods

2.1.Scaffold fabrication by DLP

Commercial powders of β-TCP (Whitlockite OD, Plasma Biotal Limited) with an average particle size of 2.36 μm, a density of 3.07 g/cm^3 and a refractive index of 1.63 [27], were suspended in a commercial acrylic resin (FTD Standard Blend 3D Printing resin, Fun To Do, Alkmaar, The Netherland). The acrylic resin employed had a density of 1.13 g/cm^3 and a refractive index of 1.5 [28], was unpigmented, but included suitable photo-initiators, curing very quickly when exposed to UV-visible light, which speeds up the printing process. However, this fact also entails certain limitations, since there is just a small window to prevent overexposure, where cure depths do not match the desired layer thickness. Therefore, a pigment was added to the mixture to act as a photo-absorber with

the aim of providing a better control over the curing process as highlighted in previous studies [24,25].

To obtain a homogeneous suspension with suitable viscosity for printing, a centrifugal planetary mixer (THINKY ARE-250) was used after adding each element to the mixture, in intervals of 5 min at 2000 rpm. After the final composition was reached, further mixing was carried out via magnetic stirring, for at least 12 h, on a hot plate heated to 50 ºC. This increased the stability and homogeneity of the mixture, yielding a lower final viscosity that allowed increasing the solid loading. The slurry composition was optimized for the fabrication of a scaffold with pore size (s_p) and strut size (s_s) (i.e. $s_p = s_s = 400$ µm), varying the ceramic powder content in the resin from 40 to 60 wt.% and printing with different exposure times and layer thickness values. As a result, the optimum powder concentration in terms of accuracy and reproducibility during printing was established to be 50 wt.%, to which 0.75 wt.% of pigment (Poinsettia, Squires Kitchen) was added to obtain the desired control over the morphology of the struts edges. For that slurry, the optimal printing parameters were an exposure time of 0.3 s for a layer thickness of 25 µm.

Digital models of porous scaffolds with cubical shape and around 6 × 6 × 6 mm^3 external dimensions were produced using a CAD software (Creo Parametric 6.0, PTC Corporation). The internal architecture had also a cubic symmetry with square-section struts in three orthogonal directions intersecting at common points like a Cartesian 3D grid. Total porosity was kept constant (~ 44 % of the total volume) but the pore and strut size were varied: $s_p = s_s$ = 300, 350, 400, 500, 600 and 700 µm (Figure 1). These model feature sizes will be used to identify each type of scaffolds throughout the manuscript. Specimens were printed using the 3DLPrinter-HD 2.0 (Robofactory, Venice, Italy) that uses UV-visible radiation

with a wavelength in the range of 400-500 nm and an intensity of 10 mW/cm^2 [29] to illuminate the bottom of a transparent vat and the printing platform suspended from the top (bottom-up technology). Layer thickness (25 µm) was selected to match the curing depth, and the models were appropriately sliced along the Z direction using the printer's software. A combination of isopropanol, sonication and compressed air was the cleaning method employed to eliminate residues of uncured slurry from the part after the printing process. After cleaning, a post-curing treatment in an UV-light oven (365 nm, Robot Factory, Mirano (VE), Italy) for 15 min was carried out to guarantee the integrity of the parts.

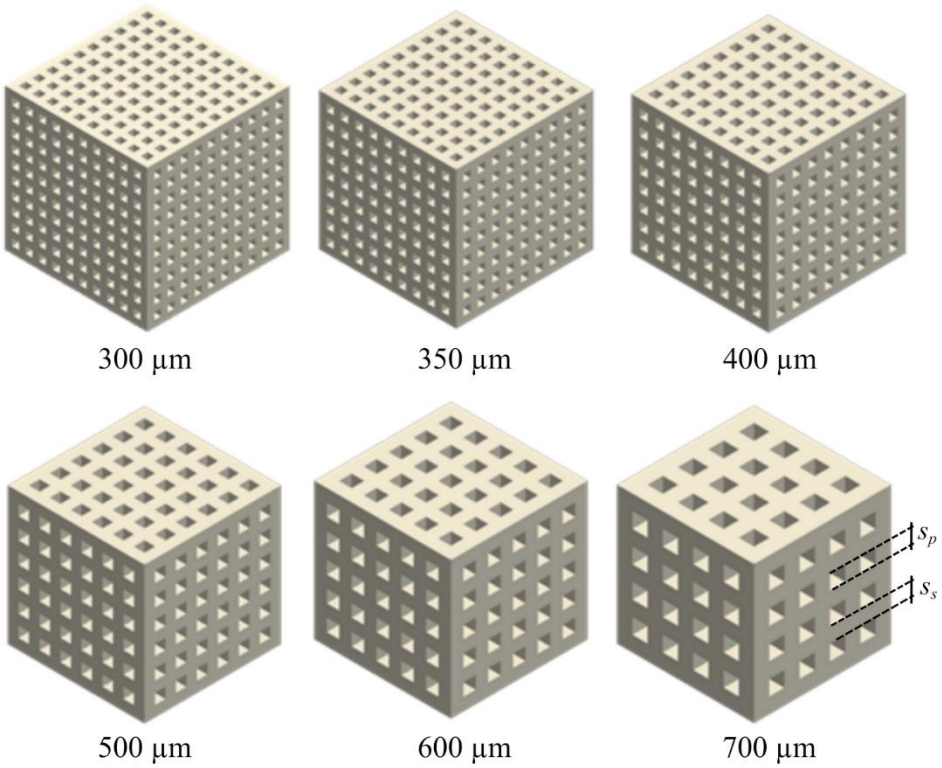

Figure 1. CAD-models used in this work for the fabrication of the different scaffolds by DLP. Labels indicate their feature (pore and strut) size, which will be used to name each type of structure throughout the manuscript.

Fully cured samples were then heat-treated in a conventional Lenton chamber furnace (Parsons Lane, Hope, UK). A two-stage treatment (debinding and sintering) was employed: first, an initial heating ramp of 0.3°C/min was used to reach 500°C, a temperature that was hold for 5 h to fully decompose the acrylic resin. Then, sintering of the ceramic samples was performed at 1200°C for 2 h, with a heating ramp of 3°C/min.

2.2.Microstructural characterization

Dimensional variations of the printed specimens with respect to the CAD file, due to light scattering from TCP particles, as well as the shrinkage due to debinding and subsequent sintering at 1200°C, were evaluated using a stereomicroscope (STEMI 2000-C, Zeiss, USA) and a scanning electron microscope (S-3600 N, Hitachi, Japan). A minimum of 15 measurements where done for each dimension at randomly chosen locations of the external surfaces of the specimens.

Apparent density values were estimated from weight and external dimensions measurements using a digital balance and caliper, respectively. Considering that the pre-designed macroporosity was around 44 vol.%, microporosity within the struts could be estimated from these density measurements. Nonetheless, mercury porosimetry (Pascal 440, Thermo Scientific, Inc) was also performed at a maximum pressure of 330 MPa to evaluate this parameter.

2.3.Mechanical testing

The compressive strength (σ_c) of the sintered specimens was determined from the maximum load registered during uniaxial compression tests. The tests were performed on a

universal testing machine (Shimadzu Autograph AG-IS) on a minimum of 5 specimens per type of sample. Loading was applied either perpendicular (⊥), or in the case of samples with $s_s = s_p = 500$ μm, also parallel (∥) to the building plane at a constant crosshead speed of 0.6 mm/min.

2.4.Simulation by Finite Element Method (FEM)

Abaqus/CAE software (2019 version, Simulia™) was used to perform simulations under a compressive load in model scaffolds with an architecture analogous to that of the specimens studied in this work. Geometrical models were developed from the CAD files used for printing (see figure 1), but the strut intersections were rounded to better simulate the actual scaffolds obtained after printing (Figure 2). Different curvature radii were used in order to analyze the effect of such parameter on the resulting stress field. Tetrahedral quadratic elements were used to mesh the whole structure with a maximum element size of 100 μm. A representative cell in the center of the structure was meshed with finer elements (10 μm) in order to improve the precision of the results. An isotropic elastic behavior was assumed for the TCP, and the elastic modulus was set to 36 GPa as in previous studies [30], although the developed stress field is independent of this parameter for a structure made of a single material, since only the strains change with the modulus. The Poisson coefficient was set to 0.22. The boundary conditions were set by defining a downward displacement of 100 μm on the upper surface of the scaffold in the direction perpendicular to that surface, and a null rotation and displacement at the opposite, bottom surface.

3. Results and discussion

Using the optimized composition of the slurry, layer thickness and exposure time indicated in the experimental section, scaffolds with different pore and strut sizes were printed to evaluate the effect of these parameters on their microstructural and mechanical performance. Figure 2 shows a representative SEM micrograph of an unsintered scaffold (after cleaning and UV curing) with 500 µm features size. In this image it is possible to visualize the individual layers stacking along the printing direction, due to the so called "stair stepping" effect typical of DLP and other AM techniques. Also, one can observe that the pores are completely open, the struts are well defined and no apparent delamination between layers exists. The main hurdle encountered in the fabrication process was the elimination of uncured slurry trapped inside the inner pores of the scaffolds, an issue that became harder to solve as the pore size decreased. As a consequence, scaffolds evaluated were limited to a minimum model pore size of 300 µm. This limitation found during the cleaning process could become very significant specially for the fabrication of large scaffolds or porous structures requiring high resolution and/or smaller pore sizes.

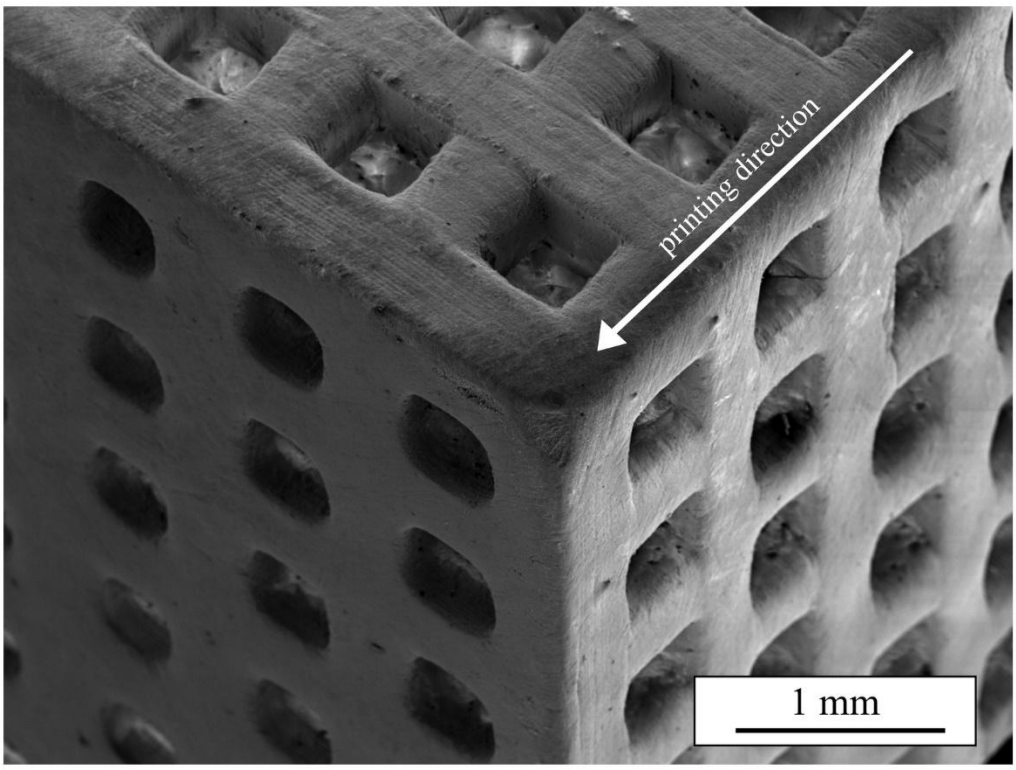

Figure 2. Printed scaffold with features size of 500 μm after cleaning and post-printing UV curing.

The dimensions of the unsintered samples (after cleaning and curing post-printing treatments) were very close (within measurement errors) to the dimensions in the CAD models, as that was the main criteria used in the optimization of the exposure conditions. As expected, however, the scaffolds shrunk significantly after sintering, as highlighted in the SEM micrographs reported in Figure 3, showing lateral views of a scaffold with 400 μm feature size before (Fig. 3a-c) and after heat-treatment (Fig. 3d-f). The microporosity that is apparent in the unsintered specimens is produced by superficial dissolution of the resin during the cleaning process and would not be found in the struts' interior. From these images, it is again possible to note that bonding between layers is apparently good, both

before and after the heat treatment, with no evidence of the interphases apart from the roughness at the external surface (Figs. 3b and 3e), which allows for the identification of individual layers.

Measurements of pore and strut size, s_p and s_s respectively, after the heat treatment are reported in Table 1. The average linear shrinkage for all samples was almost isotropic and computed to be 30 ± 1 %, as evaluated from their external dimensions before and after sintering. This large shrinkage may become an issue for the fabrication of complex structures, especially when dimensional accuracy is a requirement and the architecture of the component is not homogeneous in each direction in space, for example when trying to match the scaffold external shape to a specific patient's lesion. Small dimensional differences were found between the printing plane (XY) and the layer stacking direction (Z), with struts slightly thicker—and pores, hence, smaller—in the stacking direction. These differences, while statistically significant, were small (< 5 %) and typically below the selected layer thickness of 25 µm, in any case comparable in most cases to the experimental errors in the measurements. Therefore, they were neglected in subsequent analyses by averaging dimensional data in all directions.

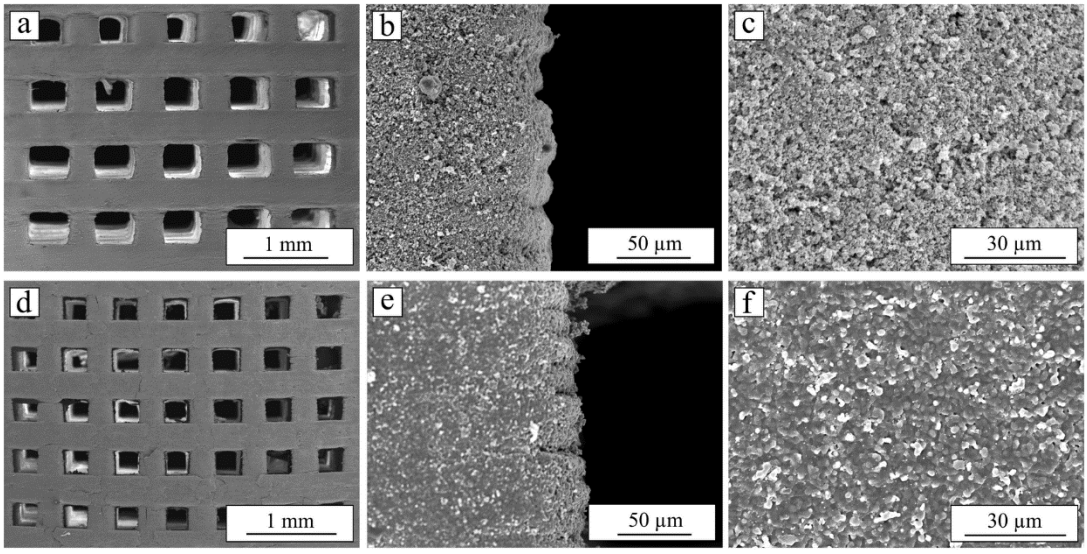

Figure 3. SEM micrographs of the surface of representative scaffolds with 400 µm model feature dimensions before (a-c) and after (d-f) heat treatment.

The aforementioned notable shrinkage after sintering was accompanied by a significant reduction of microporosity (cf. Figs. 3c and 3f). Apparent density, as shown in Figure 4, was very similar for the different scaffolds. However, statistically different values were measured in the case of structures with smaller feature dimensions (in the designed models): 300 and 350 µm. Specifically, in those cases the scaffolds were apparently slightly denser, by ~ 10 % and 6 %, respectively, than the average value for the rest of the cases; such average density was 1.44 ± 0.06 g/cm^3, which corresponded to an apparent porosity of approximately 53 ± 2%. Since, as mentioned in previous section, the designed macropores represent around 44 vol.% volumetric porosity, the rest would correspond to the microporosity within the struts. As a result, it was estimated that struts contained ~10 vol.% of pores in the case of 400, 500, 600 and 700 feature-size scaffolds, while in the 300 and 350 ones it would be ~4 to 6 vol.%, respectively.

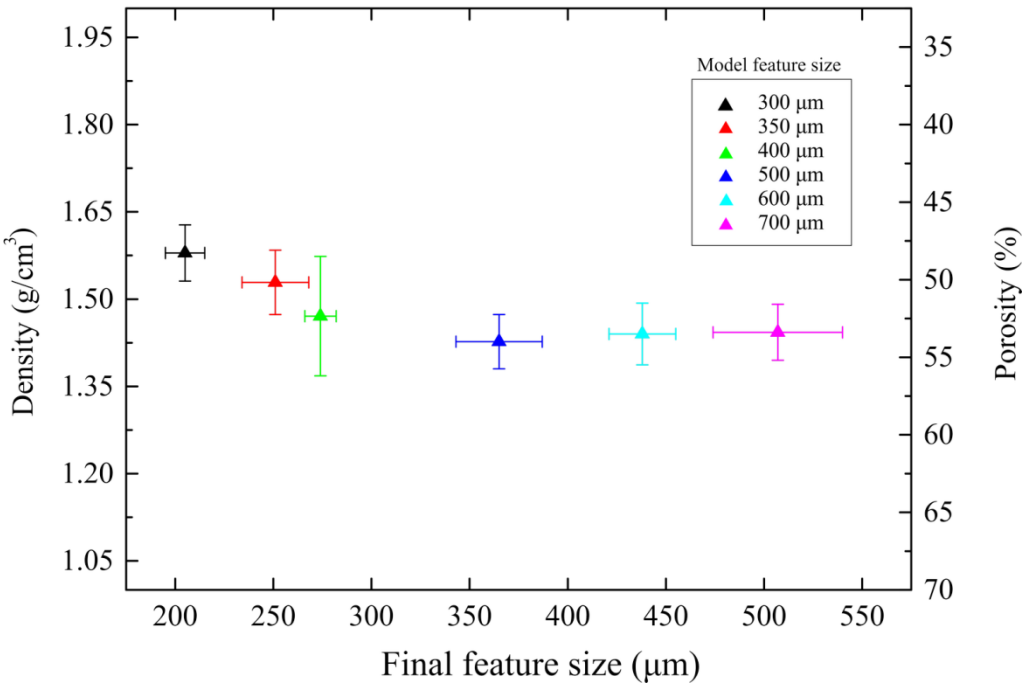

Figure 4. Apparent density and total porosity for the fabricated scaffolds after sintering, with indicated model feature dimensions. Data represent mean values with standard deviations as error.

The result provided by mercury intrusion porosimetry for the microporosity of the struts was 26 vol.%, which corresponds to a 14.6 vol.% of volumetric porosity in the scaffold, which roughly agrees with the estimations (within the large uncertainties in all these estimations) made for the scaffolds with larger pores. Also, the comparison between both estimates seems to indicate that closed porosity, if any, is not very abundant since otherwise the mercury porosimetry estimation should lie well below the previously calculated value since only the open porosity is accessible to the mercury. In any case, both estimates suggest that despite the relatively large shrinkage occurring during the heat treatment, the low green density of the fabricated scaffolds still yielded a very significant level of strut

microporosity after sintering, and although this can be beneficial in terms of biological performance of the scaffolds, it certainly limits their mechanical strength. The typical pore distribution is shown in Figure 5a, corresponding to a scaffold with 500 µm characteristic size, with most of the pores in the submicrometric range. These dimensions are in line with the SEM observations of the microstructure (Fig.3f). The secondary maximum at larger, micrometric pore sizes is attributed to surface roughness arising from layer stacking and small superficial fissures that may occur during debinding.

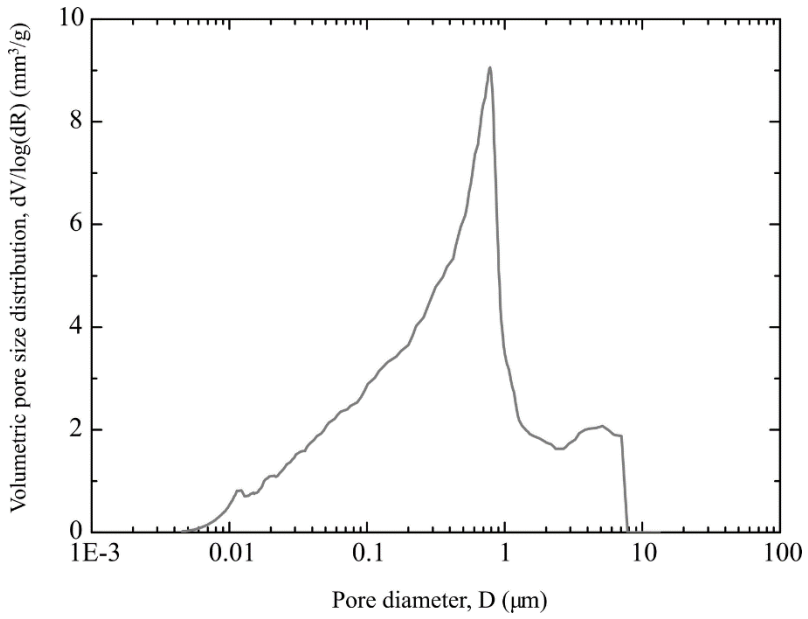

Figure 5. Representative (a) volumetric pore size distribution in a sintered scaffold with 500 µm characteristic size.

Since microporosity within the struts does not seem to depend significantly on the scaffolds feature sizes, the reason for the observed difference in density (Fig. 4) in scaffolds with smaller feature sizes should be explained by a lack of success in eliminating the excess of slurry from the inner macroporosity. This was confirmed by SEM observations of some scaffolds' midsections, as the one shown in Figure 6 for a scaffold with 300 µm

characteristic size. The additional ceramic material resulting from the sintering of the slurry trapped in the innermost pores of the scaffold, which was not removed by the post-printing cleaning procedure, is evident in this image. It should be noted that this ceramic residue coming from the incomplete removal of the slurry was observed only in the scaffolds with the smallest pore sizes (i.e. 300 and 350 μm).

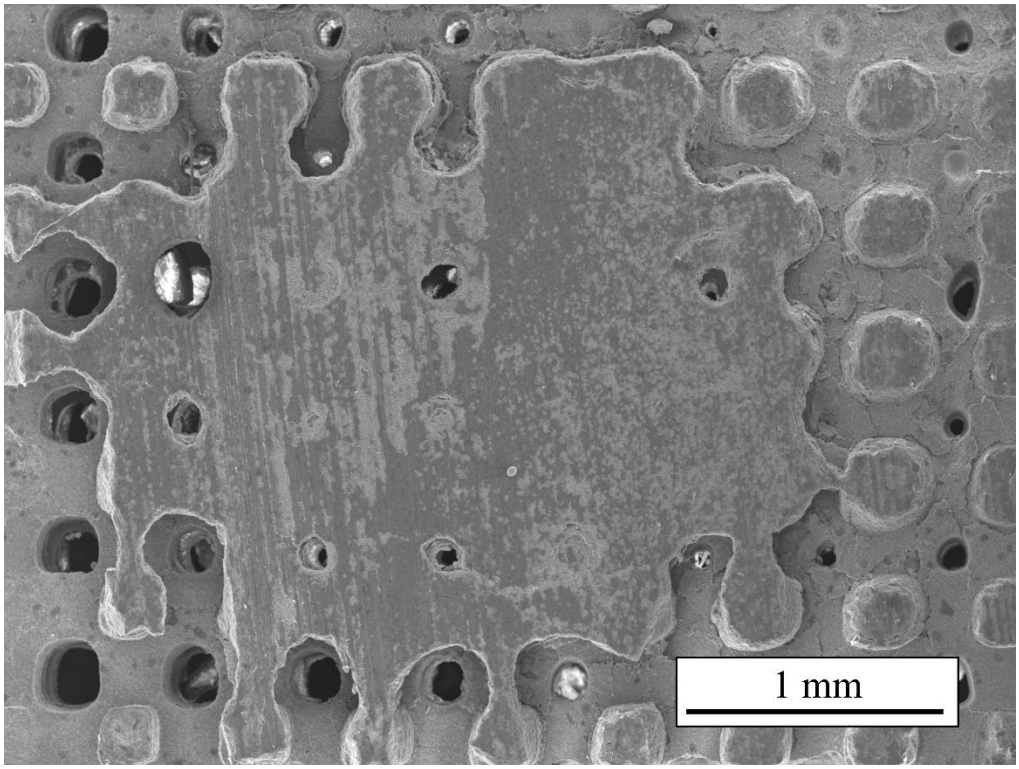

Figure 6. SEM micrograph of the transversal midsection of a scaffold with 300 μm feature size. The ceramic material resulting from the densification of the slurry occupying its inner pores can be observed.

Regarding the mechanical characterization of the scaffolds, firstly the most deleterious load configuration was identified by performing uniaxial compression tests on scaffolds with

500 µm feature size along two orthogonal directions: perpendicular (⊥) and parallel (∥) to the building/printing plane (XY). Representative examples of stress-strain curves for the two loading configurations and the mean compressive strength (σ_c) values obtained are shown in Figure 7. When the load was applied in the perpendicular direction, multiple local cracking events can be observed in the stress-strain curve even before approaching the ultimate stress (Fig. 7a). However, when the load was applied in the parallel direction failure occurred more abruptly with little sign of any previous damage to the structure. Besides, the measured compressive strength (Fig. 7b) for the parallel configuration (22 ± 4 MPa) almost doubled the value for the perpendicular configuration (12 ± 3 MPa). In both cases, the strength of the fabricated scaffolds remained above or well within the range of cancellous bone strength values.

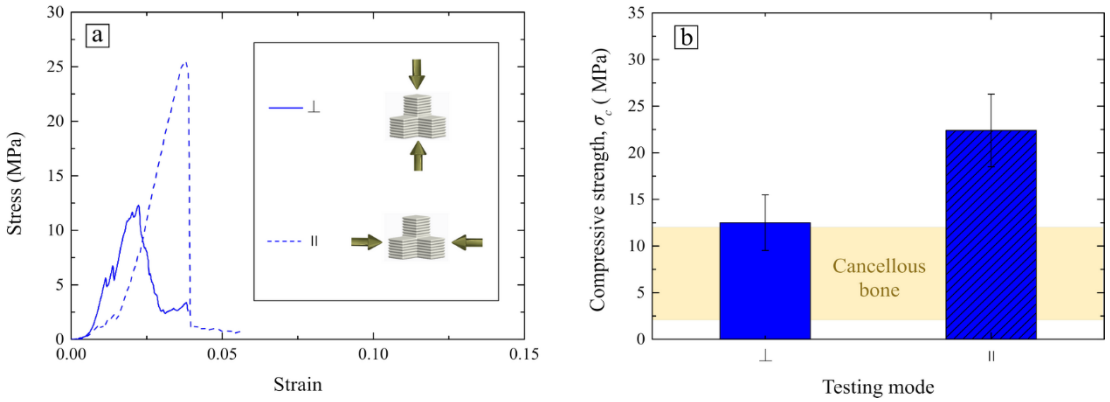

Figure 7. (a) Representative stress-strain curves and (b) mean uniaxial compressive strength (with standard deviation as error bar) for scaffolds with 500 µm feature size tested parallel and perpendicular to the printing plane as indicated. The shaded band in (b) represents typical values of human cancellous bone [31], for comparison.

Understanding why the scaffolds are weaker when tested in the perpendicular orientation is not straightforward. One might try to attribute it to the dimensional differences observed in the evaluation of the scaffold microstructure (see Table 1). However, while the struts sizes evaluated in the printing XY plane were smaller than in the Z direction—which should decrease the cross-sectional area that supports the load and make the structure weaker when tested in the perpendicular direction— the differences would only account for a ~10% increase in strength in the samples tested in the parallel orientation, far below the observed 83 % difference. On the other hand, when the stress fields developed during the compressive test were analyzed by FEM, it was found that the maximum tensile stresses concentrated along the edges created by the intersections of the struts perpendicular to the loading axis (Figure 8a).

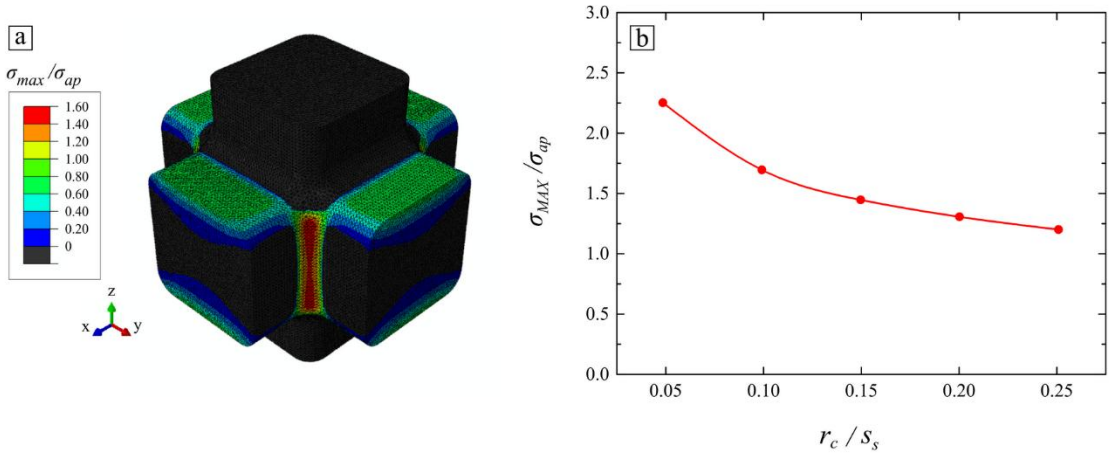

Figure 8. FEM simulation results for scaffolds under compressive loading: (a) Maximum principal stress (normalized by applied stress: $\sigma_{max} / \sigma_{ap}$) contour plot and (b) maximum tensile stress value in the structure (normalized by applied stress: $\sigma_{MAX} / \sigma_{ap}$) calculated as a

function of the radius of curvature at the strut intersections (normalized by strut size: r_c / s_s) in the FEM model.

Consequently, as indicated in Figure 8b, the value of the maximum stress in the structure, σ_{max}, is highly dependent on the radius of curvature selected for such corner, r_c, which acts as a stress concentrator. Measurements of such curvature radii in the micrographs for the 500 µm scaffolds yielded an average value of 25 ± 6 µm for the samples tested in the parallel direction —in very good agreement with the layer height selected for printing. However, a much larger 74 ± 12 µm was measured for samples tested in the perpendicular direction. The reason for that increase in the radius of curvature within the printing plane could be attributed to the light scattered during printing from the exposed regions corresponding to the two intersecting struts, which is enough to cause polymerization of the resin at such corners. Consequently, the larger curvature of the edges within the printing plane should reduce the stress concentration and, thus, increase the compressive strength of the scaffolds (by ~ 50 %) when tested perpendicularly to that plane, not diminish it. Moreover, this curvature would also increase the effective area supporting the load when testing in the orthogonal direction, effectively countering the reduction in the area associated to smaller struts.

Therefore, the explanation for the observed results must be found not in differences in the stress fields developed under each loading configuration, but on the flaw population leading to failure (i.e. the material intrinsic strength) in each case. The intrinsic strength of a polycrystalline material such as β-TCP is typically an isotropic magnitude. However, when the material is built layer by layer, as in 3D printing technologies such as DLP, a new

defect population may be generated at the interfaces between layers (and printing lines, in the case of other additive manufacturing techniques such as Direct Ink Writing), which can lead to a significant anisotropy in the material intrinsic strength [32,33] and toughness [34]. These fracture controlling defects cannot be, however, exclusively the interlayer surface grooves that are apparent in Fig. 3, since propagation of cracks in mode I (preferred in brittle materials) from those surface flaws would be more favorable when testing in the parallel orientation. Layered structures are typically found to be weaker when tested perpendicular to the stacked layers in compression because the presence of defects across the whole interlayer favors shear-driven delamination [32]. Unlike tensile stresses, which are localized exclusively at the surface of the struts (Fig. 9a), shear stresses remain high throughout the struts' sections (Fig. 9b), facilitating crack initiation and propagation.

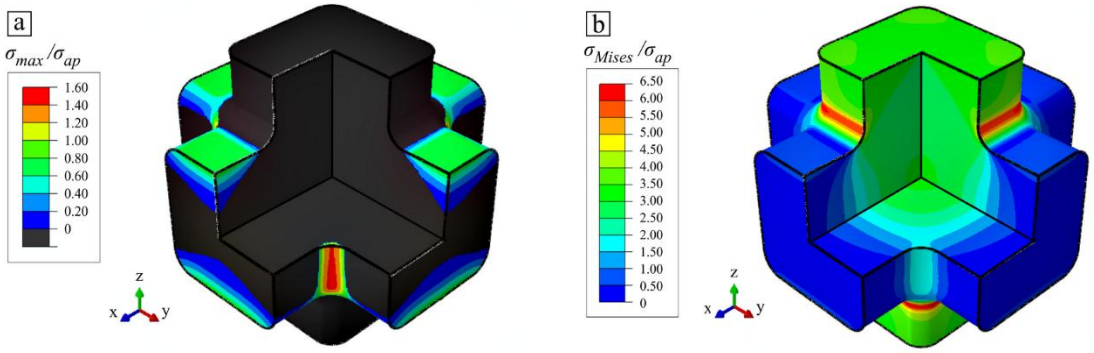

Figure 9. FEM simulation results for scaffolds under compressive loading: (a) Maximum principal stress, σ_{max}, and (b) von Mises stress, σ_{Mises}, contour plots. Stress values have been normalized by the applied stress, σ_{ap}.

These defects are not evident in cross-sectional SEM micrographs (Fig. 10), where individual layers can be discerned only at the surface of the struts, even in polished sections (Fig. 10d). Nonetheless, their presence might explain also why the struts dimensions were slightly larger in the Z direction (Table 1). Moreover, the existence of interlayer defects in parts manufactured by vat photopolymerization techniques (DLP) have also been recently reported [35].

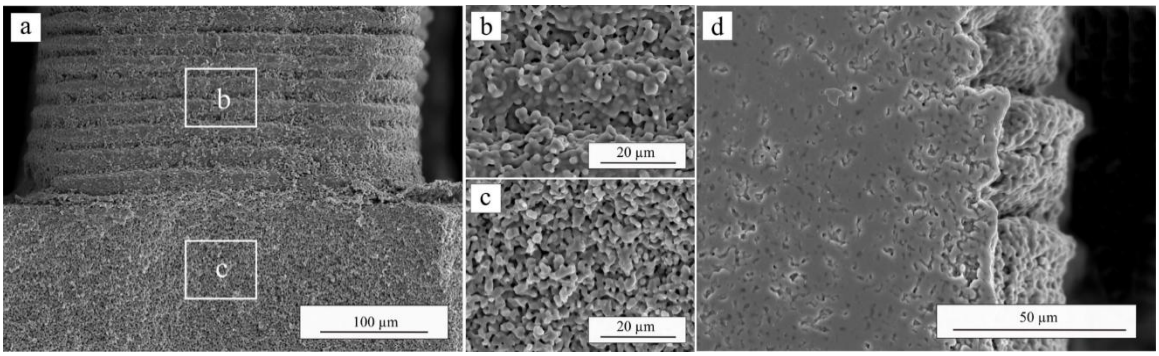

Figure 10. Cross-sectional SEM micrographs of a scaffold fractured perpendicularly to the printing plane (a-c) before and (d) after polishing. Layer grooves are evident at the surface of the struts, but no interlayers defects can be found towards the strut's interior.

According to this hypothesis, the reduction in strength when compressing perpendicularly to the printing plane would be due to the generation of local interlayer shear cracks that facilitate the progressive failure of the structure. The occurrence of these local cracks was apparent already in the serrated stress-strain curves of specimen tested in the perpendicular orientation (Fig. 7a), but is more clearly appreciated in the *postmortem* SEM micrographs shown in Fig. 11. In this fractured specimen, the longitudinal cracking of the struts along

the intersections that was predicted by the FEM stress contours (Fig. 8a) are observed perpendicular to the image. But, more importantly, it is evident that there is also extensive fracture on the vertical struts (those perpendicular to the image in Fig.11a). Those struts are fractured diagonally, as corresponding to a shear driven mechanism, with multiple evidence of steps in the fracture surface (Fig. 11b) as expected from a laminated material with weak interlayers. Indeed, micrographs taken in the transversal direction (Fig. 11c) show cracks forming an hourglass shape typically found in this type of shear driven failure of laminated ceramic materials [32]. Such failures can occur locally at much lower stresses than required for longitudinal cracks propagation, and they reduce the overall structure resistance by diminishing the effective area of the scaffold sustaining the applied load. This does not occur when testing parallel to the printing plane where all the stacked layers support the load until a longitudinal crack can propagate through one of the interlayers at the struts' intersections. Of course, once that happens failure is catastrophic (Fig. 7a), but the stress required for this crack to initiate propagation throughout the structure is higher than for failure in the perpendicular orientation.

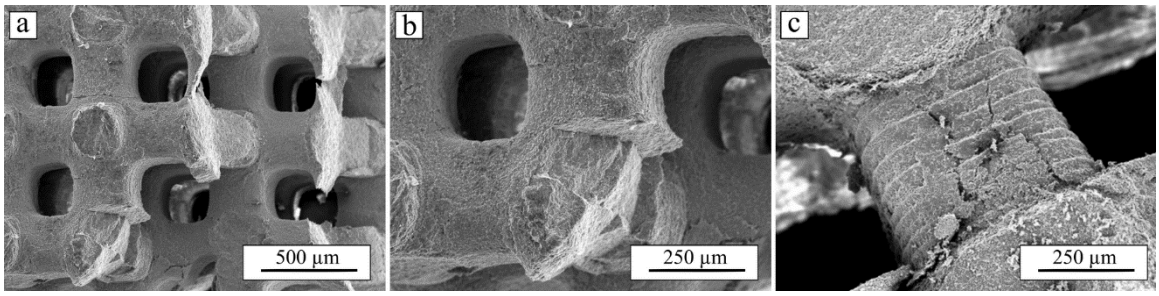

Figure 11. SEM micrographs of a fractured scaffold after a uniaxial compression test in the direction perpendicular to the printing plane: (a) Top view showing crack propagation both orthogonal to the printing plane but also diagonally through the vertical struts, with (b) evidence of steps produced by interlayer cracking and (c) hourglass shaped cracks in the transversal orientation, typical of shear driven failure.

Although, to the best of our knowledge, this anisotropy in the compressive strength had not been previously reported in the literature for ceramics materials fabricated by DLP, the magnitude of the weakening due to interlayer defects seems to be quite significant for the materials developed in this study. Indeed, it more than compensates the effect of the curvature at the struts intersections that would have tended to make the scaffolds stronger when compressed in the perpendicular direction. Instead, the structure resulted to be ~55 % weaker under that load configuration. These results indicate that ceramic components fabricated by DLP, regardless of their geometry, will be weaker when compressed perpendicularly to the printing plane due to interlayer shear failure. Minimizing the interlayer defects responsible for this failure should be a major focus of any future research aimed at further enhancing the mechanical performance of these components. Improving

densification through the optimization of the solid content in the resins' slurries and the debinding process for resin elimination in each formulation should be beneficial in this regard. Indeed, existing studies in ceramics materials such as alumina and zirconia, which can be fully densified, fabricated by vat photopolymerization techniques report a much more reduced anisotropy in their (bending) strength, and how this anisotropy diminishes with densification and surface polishing [35,36]. Moreover, improving the stabilization of the ceramic particles in the acrylic polymer, to avoid potential sedimentation during printing, which would lead to a polymer-rich top region in each layer generating interlayer porosity and delamination after debinding and sintering, should also be pursued. The effect of other printing parameters such as exposure time and layer thickness should be also analysed in detail in future work

Scaffolds for all remaining feature sizes were tested perpendicular to the printing plane since this was the most deleterious configuration. Representative stress-strain curves and resulting mean compressive strength values are shown in Figure 12a. All scaffolds exhibited a brittle behavior and after the maximum stress was reached, the curve dropped progressively down to zero, as expected. However, scaffolds with the two smallest feature sizes were able to sustain the load for a much longer period after the peak stress thanks to the denser core formed by the slurry trapped within the innermost pores. Nonetheless, as shown in Fig. 12b, the compressive strength does not significantly ($p > 0.5$) change with the feature size of the scaffolds and all values lay close to the upper limit of the cancellous bone range [31], at an average value of 12 ± 3 MPa. These results suggest that varying the dimensions of pores and bars, at least within the range of values analyzed here, does not have any significant influence in the final resistance of the parts.

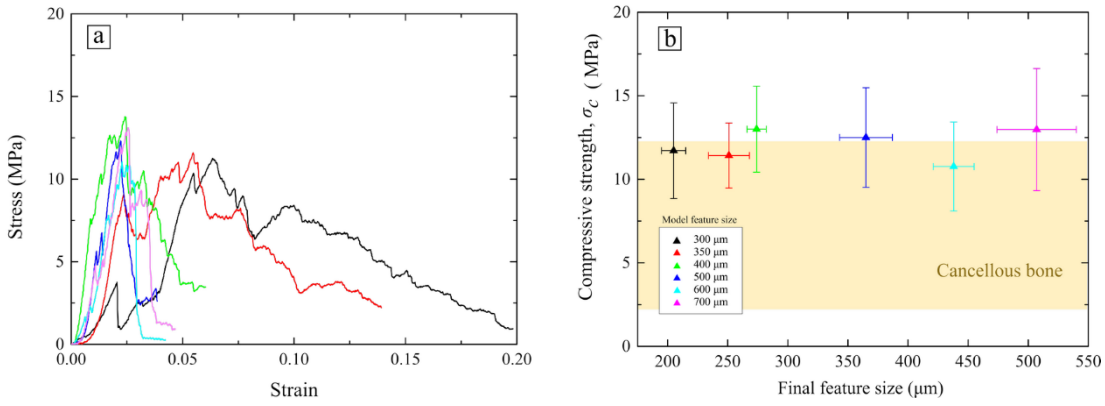

Figure 12. (a) Representative load-displacement curves and (b) mean compressive strength as a function of scaffold's feature size (with standard deviations as error bars), as evaluated in uniaxial compression tests with the load applied perpendicularly to the printing plane. The shaded band represents typical values of human cancellous bone [31], for comparison.

This is somewhat unexpected since the strength of individual struts should typically decrease with increasing size according to Weibull's theory of fracture on brittle materials [37]. This size effect has been also previously reported in scaffolds by Sabree *et al.* [38]. but it is certainly not reproduced in the present work. The most likely explanation would be that fracture in DLP scaffolds is controlled by a population of large defects introduced by the fabrication process itself which does not vary with the scaffolds feature size. Surface grooves associated to layer stacking (see Figs. 3b and 3e) are certainly to be considered representative of such critical defects, in agreement with the proposed fracture mechanism through interlayer shear failure. Defects associated to the cleaning process could also be responsible for both this lack of size effect and the large scattering in the mechanical results. Indeed, the difficulty and, thus, the duration of the cleaning process increases as the pore size diminishes; moreover, a longer exposure to the solvent and air flows used during

cleaning could produce larger defects in the struts, which would mask the Weibull size effect. However, no strong evidence was found neither in the SEM micrographs nor in the porosimetry data available to convincingly support this latter explanation. Nonetheless, clarifying this matter completely would require further research to corroborate the findings in other systems and using larger datasets. Using ceramic scaffolds with a higher toughness or improved green density may lead to lower scattering in the strength data which could simplify the analysis of the size effect, which for the size range explored here might well be within the data scattering in this work. In any case, the results of this study suggest that the DLP technique allows for the fabrication of cellular components with fully open and interconnected porosity, when printing with a design pore size larger than ~400 μm, and a known strength which would depend only on the amount of volumetric porosity and not on the chosen pore size.

4. Conclusions

Ceramic suspensions for Direct Light Processing, obtained by adding 50 wt.% of β-TCP powder as filler to an acrylic resin were successfully employed to fabricate bioactive scaffolds composed of interpenetrating square-section struts with dimensions varying from 300 to 700 μm but with comparable volumetric microporosity. Elimination of uncured resin trapped within the pores became a significant limitation of this technique in the fabrication of scaffolds with small pore sizes: traces of uncured resin remained trapped in the inner pores—even in pores as large as 350 μm—a problem that is expected to worsen with increasing the size of the printed component. The low volumetric solid content (~25 vol.%)

of the suspensions is also of some concern. Scaffolds fabricated here underwent a large (30 %) linear shrinkage after heat treatment, which may become an issue for the fabrication of complex structures, especially when dimensional accuracy is a requirement. Low green density can also limit mechanical performance, especially in materials that are difficult to densify. In the case of the micrometric TCP powder used here ~25 vol.% microporosity remained within the struts after sintering. And although this can be beneficial in terms of cell attachment and proliferation, it certainly limits the mechanical performance of the structure. Besides, the results of the mechanical tests performed point towards the presence of interlayer defects inducing shear failure in the structures under compression perpendicular to the printing plane, which thus becomes the most deleterious loading configuration for these scaffolds. Nevertheless, the compressive strength of the fabricated scaffolds was comparable to that of cancellous bone [31], even when tested perpendicular to the printing plane. Unexpectedly, the scaffold strength was found to be independent of the strut and pore sizes, or at least the effect was undetectable within the data scattering. This lack of effect could be attributed to defects of fixed size and location controlling failure; these defects can be identified in the surface steps which are typical of this layer-by-layer additive manufacturing technique (DLP). Future research should focus on increasing solid content in the resins in order to minimize shrinkage and enhance mechanical performance of the scaffolds and, of course, their biological performance should also be assessed.

5. Acknowledgements

This work was supported by the Spanish Ministerio de Ciencia, Innovación y Universidades, co-funded by the European Regional Development Funds [grants RTI2018-095566-B-I00 (MCIU/AEI/FEDER, UE) and MAT2015-64670-R (MINECO/FEDER, UE)].

6. References

[1] M. Bohner, Resorbable biomaterials as bone graft substitutes An ageing population and the democratization of high-risk sports have, Mater. Today. 13 (2010) 24–30. doi:10.1016/S1369-7021(10)70014-6.

[2] H.R. Piehler, The Future of Medicine, MRS Bull. 25 (2000) 67–70. doi:https://10.1038/scientificamerican0413-48.

[3] R. Langer, J.P. Vacanti, N. Series, N. May, Tissue Engineering, 260 (2008) 920–926. doi:https://10.1126/science.8493529.

[4] S. Bose, S. Vahabzadeh, A. Bandyopadhyay, Bone tissue engineering using 3D printing, Mater. Today. 16 (2013) 496–504. doi:https://10.1016/j.mattod.2013.11.017.

[5] N. Travitzky, A. Bonet, B. Dermeik, T. Fey, I. Filbert-Demut, L. Schlier, T. Schlordt, P. Greil, Additive manufacturing of ceramic-based materials, in: Adv. Eng. Mater., 2014: pp. 729–754. doi:10.1002/adem.201400097.

[6] P. Miranda, A. Pajares, E. Saiz, A.P. Tomsia, F. Guiberteau, Mechanical properties

of calcium phosphate scaffolds fabricated by robocasting, J. Biomed. Mater. Res. Part A. (2007). doi:https://10.1002/jbm.a.31587.

[7] A.J. Salinas, M. Vallet-Regí, Bioactive ceramics : from bone grafts to tissue, RSC Adv. (2013) 3, 11116. doi:https://10.1039/c3ra00166k.

[8] G. Daculsi, O. Laboux, O. Malard, P. Weiss, Current state of the art of biphasic calcium phosphate bioceramics, J. Mater. Sci. Mater. Med. 14 (2003) 195–200. doi:10.1023/A:1022842404495.

[9] I. D Thompson, L. L Hench, Mechanical Properties of Bioactive Glasses, Glass-Ceramics and Composites, 1998. doi:https://10.1243/0954411981533908.

[10] V. Karageorgiou, D. Kaplan, Porosity of 3D biomaterial scaffolds and osteogenesis, Biomaterials. 26 (2005) 5474–5491. doi:https://10.1016/j.biomaterials.2005.02.002.

[11] S. A Skoog, P.L. Goering, J. Narayan, U.S. Food, J. Narayan, Stereolithography in tissue engineering, 2013. doi:10.1007/s10856-013-5107-y.

[12] Z. Chen, Z. Li, J. Li, C. Liu, C. Lao, Y. Fu, C. Liu, Y. Li, P. Wang, Y. He, 3D printing of ceramics : A review, J. Eur. Ceram. Soc. 39 (2019) 661–687. doi:10.1016/j.jeurceramsoc.2018.11.013.

[13] S. Eqtesadi, A. Motealleh, P. Miranda, A. Pajares, A. Lemos, J.M.F. Ferreira, Robocasting of 45S5 bioactive glass scaffolds for bone tissue engineering, J. Eur. Ceram. Soc. 34 (2014) 107–118. doi:10.1016/j.jeurceramsoc.2013.08.003.

[14] F.J. Martínez-Vázquez, F.H. Perera, P. Miranda, A. Pajares, F. Guiberteau, Improving the compressive strength of bioceramic robocast scaffolds by polymer

infiltration, Acta Biomater. 6 (2010) 4361–4368. doi:10.1016/j.actbio.2010.05.024.

[15] Y. Zeng, Y. Yan, H. Yan, C. Liu, Biomaterials 3D printing of hydroxyapatite scaffolds with good mechanical and biocompatible properties by digital light processing, J. Mater. Sci. 53 (2018) 6291–6301. doi:10.1007/s10853-018-1992-2.

[16] R. Felzmann, S. Gruber, G. Mitteramskogler, P. Tesavibul, A.R. Boccaccini, R. Liska, J. Stampfl, Lithography-based additive manufacturing of cellular ceramic structures, in: Adv. Eng. Mater., 2012: pp. 1052–1058. doi:10.1002/adem.201200010.

[17] V.S.D. Voet, T. Strating, G.H.M. Schnelting, P. Dijkstra, M. Tietema, J. Xu, A.J.J. Woortman, K. Loos, J. Jager, R. Folkersma, Biobased Acrylate Photocurable Resin Formulation for Stereolithography 3D Printing, ACS Omega. 3 (2018) 1403–1408. doi:10.1021/acsomega.7b01648.

[18] M.L. Griffith, J.W. Halloran, Freeform Fabrication of Ceramics via Stereolithography, J. Am. Ceram. Soc. 79 (1996) 2601–608.

[19] A. Badev, Y. Abouliatim, T. Chartier, L. Lecamp, P. Lebaudy, C. Chaput, C. Delage, Photopolymerization kinetics of a polyether acrylate in the presence of ceramic fillers used in stereolithography, J. Photochem. Photobiol. A Chem. 222 (2011) 117–122. doi:10.1016/j.jphotochem.2011.05.010.

[20] R. He, W. Liu, Z. Wu, D. An, M. Huang, H. Wu, Q. Jiang, X. Ji, S. Wu, Z. Xie, Fabrication of complex-shaped zirconia ceramic parts via a DLP- stereolithography-based 3D printing method, Ceram. Int. 44 (2018) 3412–3416. doi:10.1016/j.ceramint.2017.11.135.

[21] Y. Lee, J. Lee, W. Maeng, Y. Koh, H. Kim, Journal of the European Ceramic Society Photocurable ceramic slurry using solid camphor as novel diluent for conventional digital light processing (DLP) process, J. Eur. Ceram. Soc. 39 (2019) 4358–4365. doi:10.1016/j.jeurceramsoc.2019.05.069.

[22] F. Scalera, C.E. Corcione, F. Montagna, A. Sannino, A. Maffezzoli, Development and characterization of UV curable epoxy / hydroxyapatite suspensions for stereolithography applied to bone tissue engineering, Ceram. Int. 40 (2014) 15455–15462. doi:10.1016/j.ceramint.2014.06.117.

[23] V.I. Putlyaev, P. V. Evdokimov, T. V. Safronova, E.S. Klimashina, N.K. Orlov, Fabrication of osteoconductive Ca3–x M2x (PO4)2 (M = Na, K) calcium phosphate bioceramics by stereolithographic 3D printing, Inorg. Mater. 53 (2017) 529–535. doi:10.1134/s0020168517050168.

[24] J. Schmidt, H. Elsayed, E. Bernardo, P. Colombo, Digital light processing of wollastonite-diopside glass-ceramic complex structures, J. Eur. Ceram. Soc. 38 (2018) 4580–4584. doi:10.1016/j.jeurceramsoc.2018.06.004.

[25] H. Elsayed, J. Schmidt, Bioactive glass-ceramic scaffolds by additive manufacturing and sinter-crystallization of fine glass powders, (2018) 6–10. doi:10.1557/jmr.2018.120.

[26] R. Gmeiner, G. Mitteramskogler, J. Stampfl, A.R. Boccaccini, Stereolithographic ceramic manufacturing of high strength bioactive glass, Int. J. Appl. Ceram. Technol. 12 (2015) 38–45. doi:10.1111/ijac.12325.

[27] P.J. Scully, A. Baum, D. Liu, W. Perrie, Refractive Index Structures in Polymers

Refractive Index Structures in Polymers, 2012. doi:10.1007/978-3-642-23366-1.

[28] p. 4-49 Lide, D.R. (ed). CRC Handbook of Chemistry and Physics. 72nd ed. Boca Raton, FL: CRC Press, 1991-1992., No Title, (n.d.).

[29] O. Santoliquido, P. Colombo, A. Ortona, Additive Manufacturing of ceramic components by Digital Light Processing: A comparison between the "bottom-up" and the "top-down" approaches, J. Eur. Ceram. Soc. 39 (2019) 2140–2148. doi:https://doi.org/10.1016/j.jeurceramsoc.2019.01.044.

[30] F.J. Martínez-Vázquez, F.H. Perera, P. Miranda, A. Pajares, F. Guiberteau, Improving the compressive strength of bioceramic robocast scaffolds by polymer infiltration, Acta Biomater. 6 (2010) 4361–4368. doi:https://10.1016/j.actbio.2010.05.024.

[31] L.L. Hench, Biomaterials, Artificial Organs and Tissue Engineering, in: L.L. Hench, J.R.B.T.-B. Jones (Eds.), Woodhead Publ. Ser. Biomater., 2005: pp. 79–89. doi:https://doi.org/10.1533/9781845690861.2.79.

[32] P. Feng, X. Meng, J. Chen, L. Ye, Mechanical properties of structures 3D printed with cementitious powders, Constr. Build. Mater. 93 (2015) 486–497. doi:10.1016/j.conbuildmat.2015.05.132.

[33] E. Feilden, E. García-tu, F. Giuliani, E. Saiz, L. Vandeperre, Journal of the European Ceramic Society Robocasting of structural ceramic parts with hydrogel inks, 36 (2016) 2525–2533. doi:10.1016/j.jeurceramsoc.2016.03.001.

[34] T.G.T. Nindhia, J. Schlacher, T. Lube, Fracture Toughness (K IC) of Lithography Based Manufactured Alumina Ceramic, IOP Conf. Ser. Mater. Sci. Eng. 348 (2018).

doi:10.1088/1757-899X/348/1/012022.

[35] J. Schlacher, T. Lube, W. Harrer, G. Mitteramskogler, M. Schwentenwein, R. Danzer, Strength of additive manufactured alumina, J. Eur. Ceram. Soc. (2020) 1–9. doi:10.1016/j.jeurceramsoc.2020.03.073.

[36] M. Saâdaoui, F. Khaldoun, J. Adrien, H. Reveron, J. Chevalier, X-ray tomography of additive-manufactured zirconia : Processing defects – Strength relations, J. Eur. Ceram. Soc. 40 (2020) 3200–3207. doi:10.1016/j.jeurceramsoc.2019.04.010.

[37] W.J. Weibull, A statistical distribution function of wide applicability, J. Appl. Mech. (1951) 293–299.

[38] I. Sabree, J.E. Gough, B. Derby, Mechanical properties of porous ceramic scaffolds : Influence of internal dimensions, 41 (2015) 8425–8432. doi:10.1016/j.ceramint.2015.03.044.

Table 1. Scaffolds' feature (pore and strut) dimensions evaluated after sintering.

Model size (µm)	**Strut size (µm)**		**Pore size (µm)**		**Average feature size (µm)**
	XY directions	Z direction	XY directions	Z direction	
300	201 ± 12	207 ± 3	214 ± 6	200 ± 5	205 ± 10
350	238 ± 25	262 ± 6	252 ± 13	255 ± 9	251± 17
400	274 ± 3	276 ± 5	275 ± 10	271 ± 9	274 ± 8
500	344 ± 19	363 ± 12	386 ± 14	367 ± 16	365 ± 22
600	422 ± 20	446 ± 7	451 ± 10	432 ± 12	438 ± 17
700	467 ± 14	532 ± 14	540 ± 20	500 ± 9	507 ± 33

Figure 1

Click here to download high resolution image

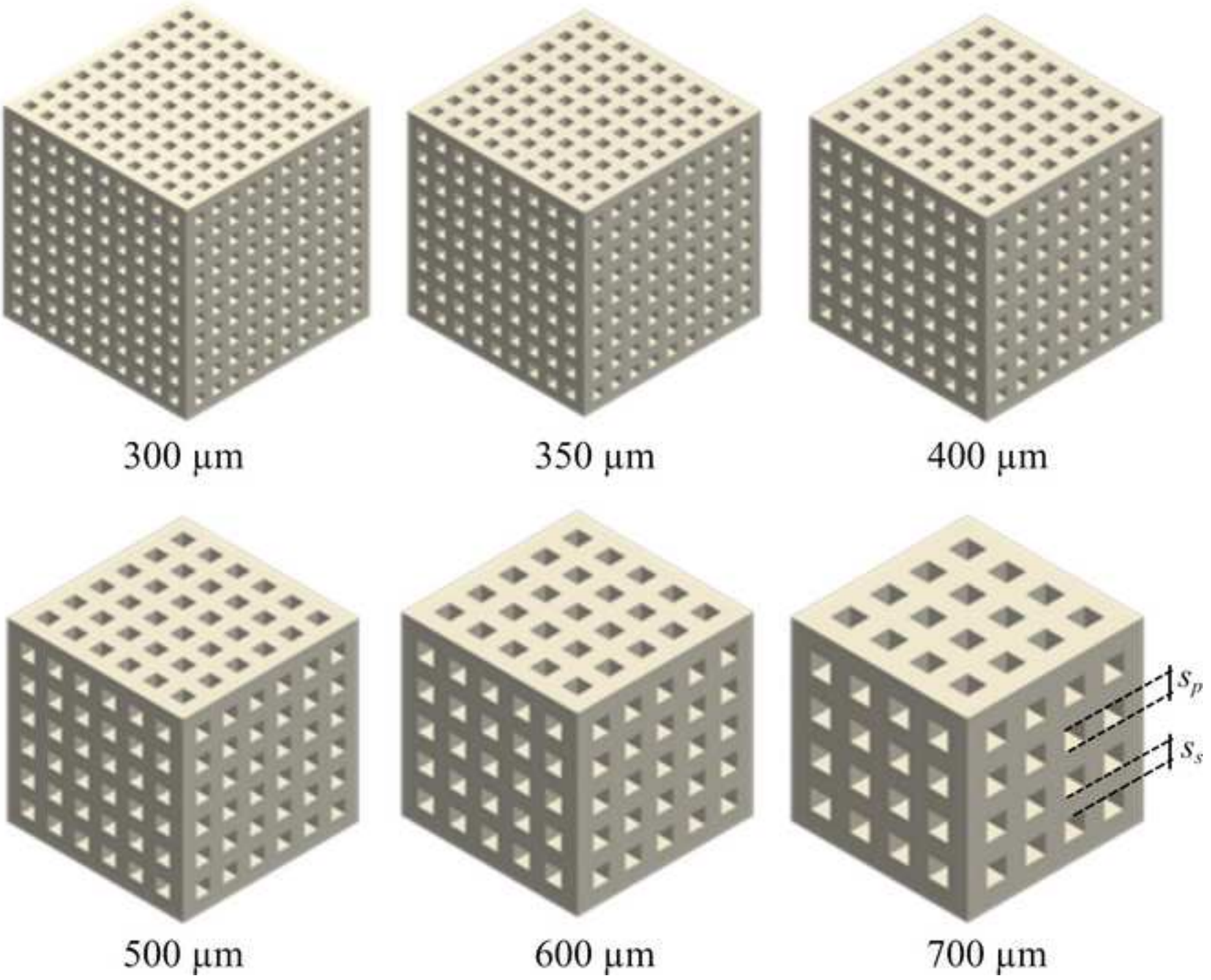

Figure 2

Click here to download high resolution image

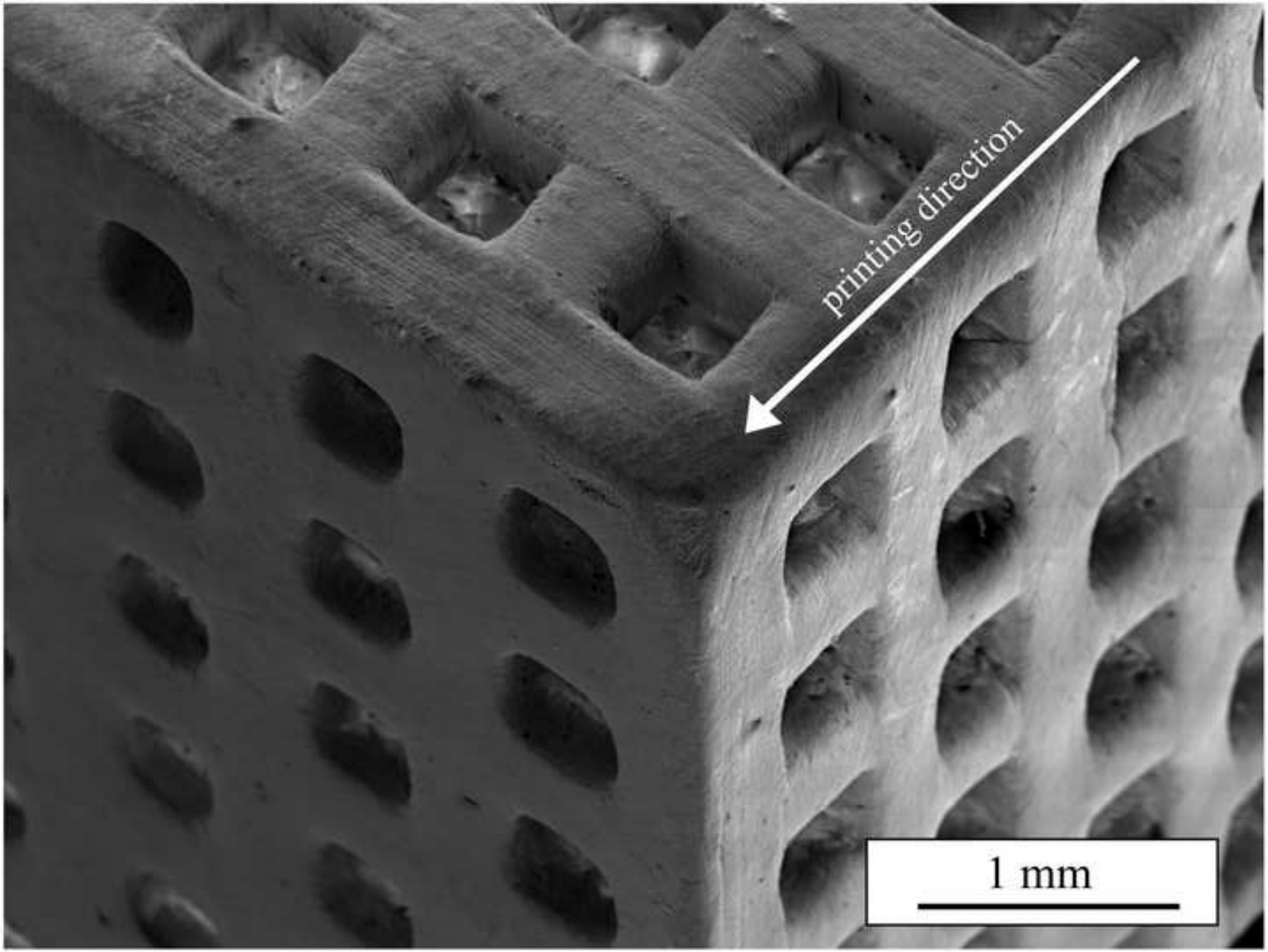

Figure 3

Click here to download high resolution image

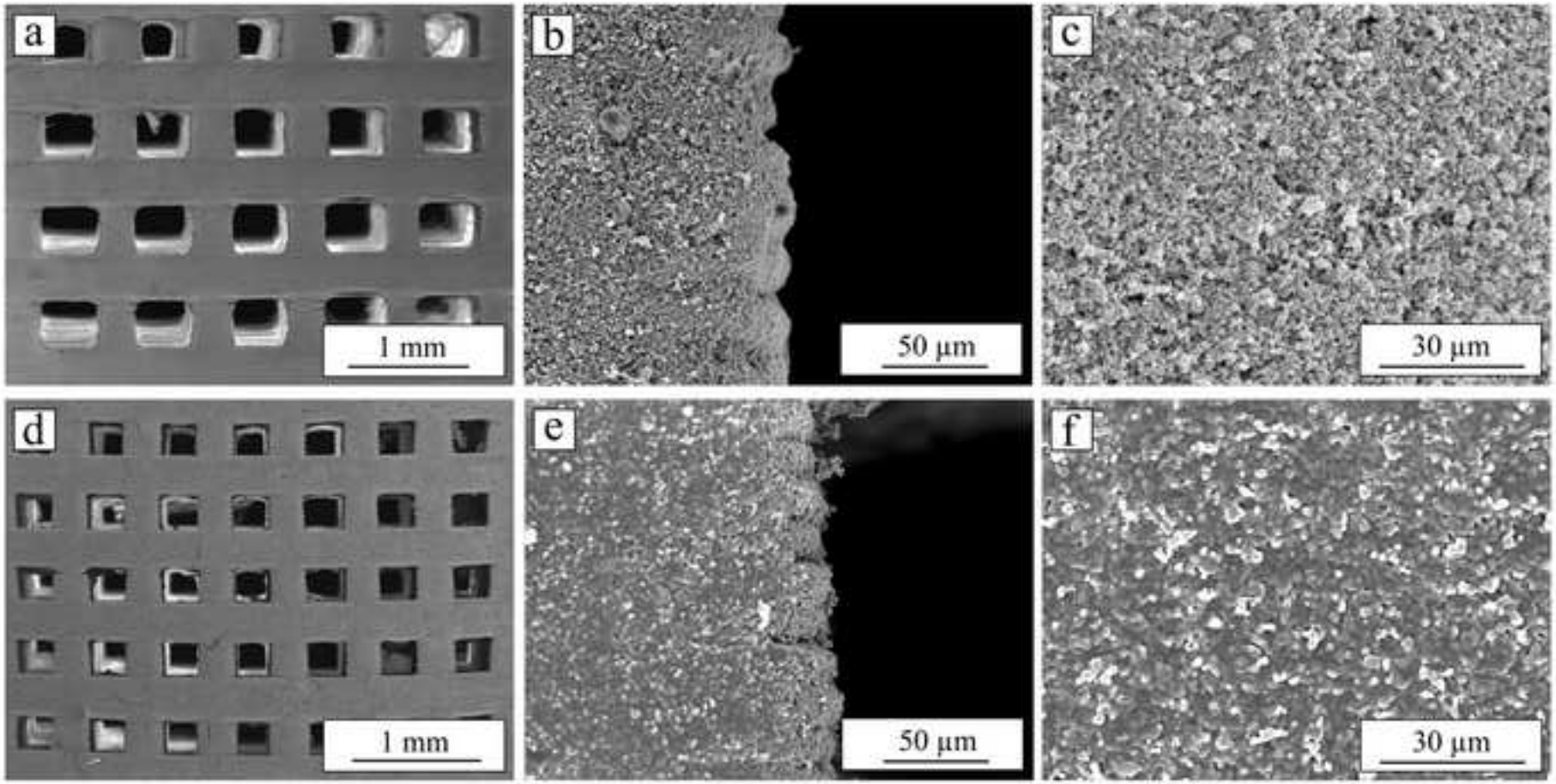

Figure 4
Click here to download high resolution image

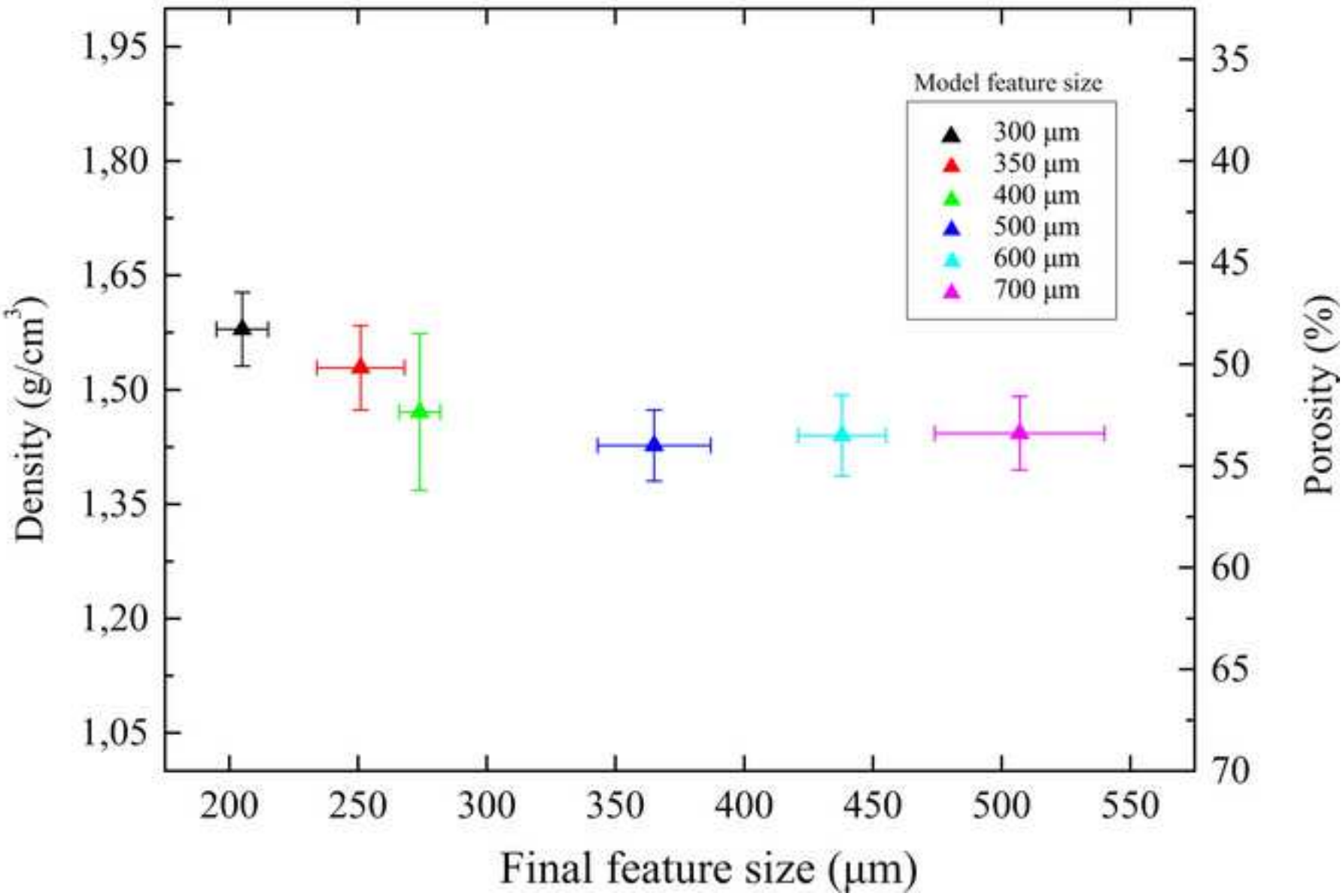

Figure 6

Click here to download high resolution image

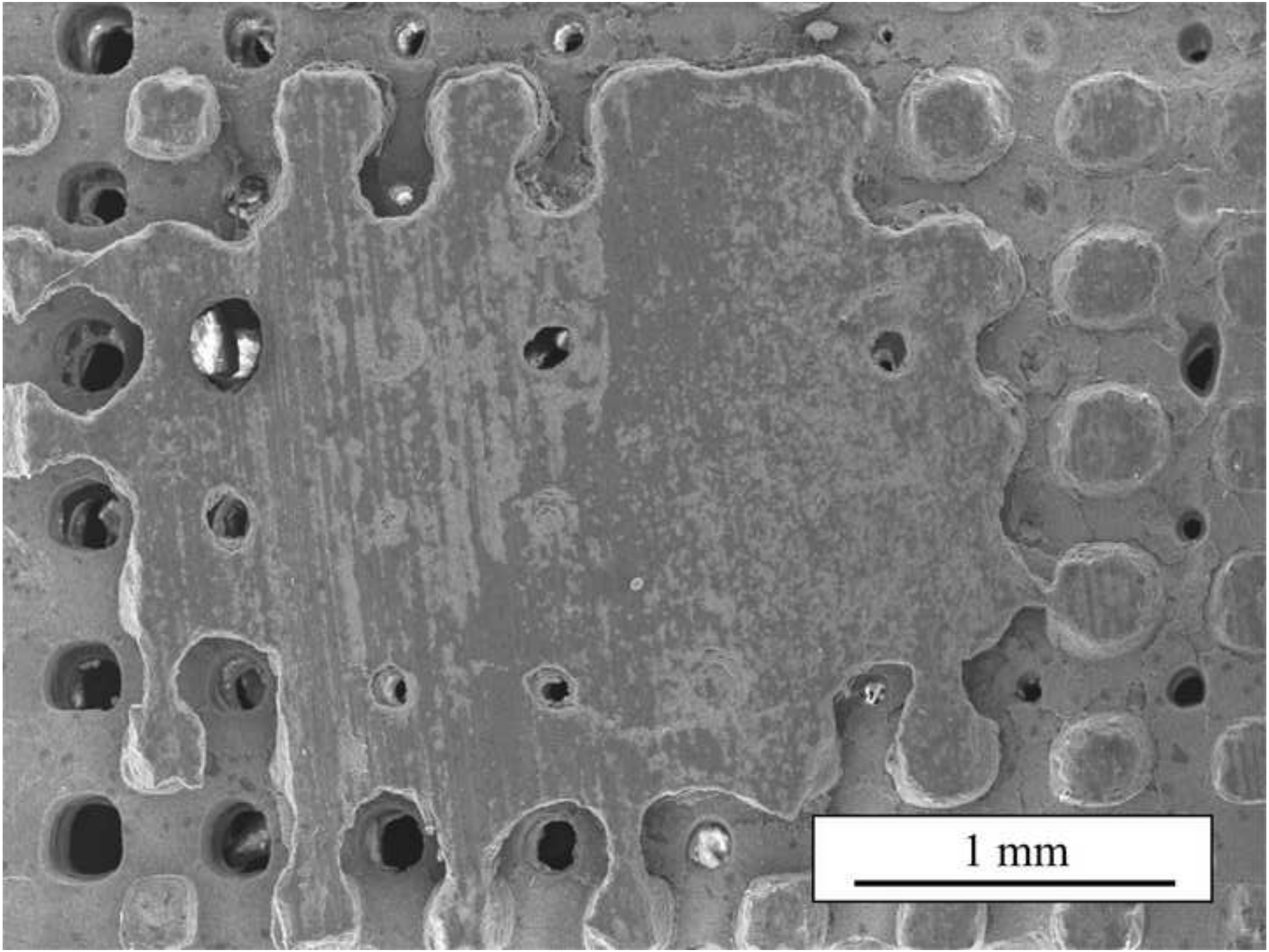

Figure 5

Click here to download high resolution image

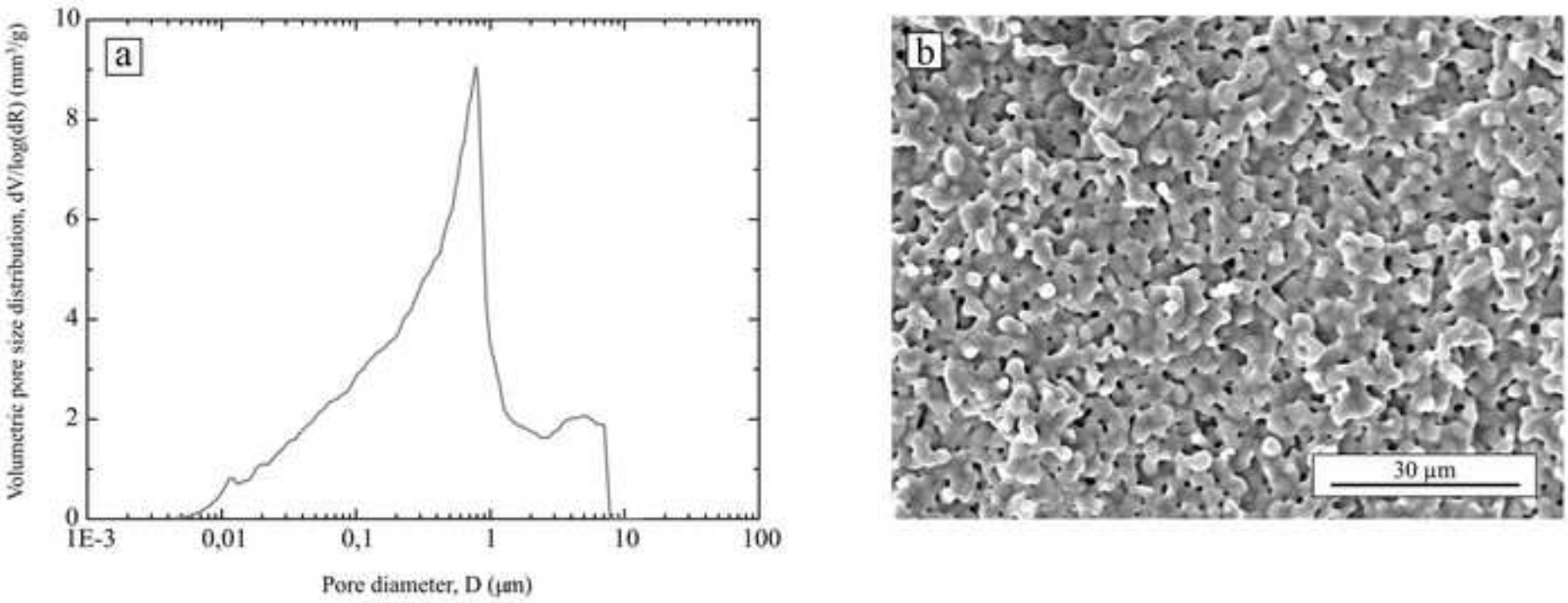

Figure 7

Click here to download high resolution image

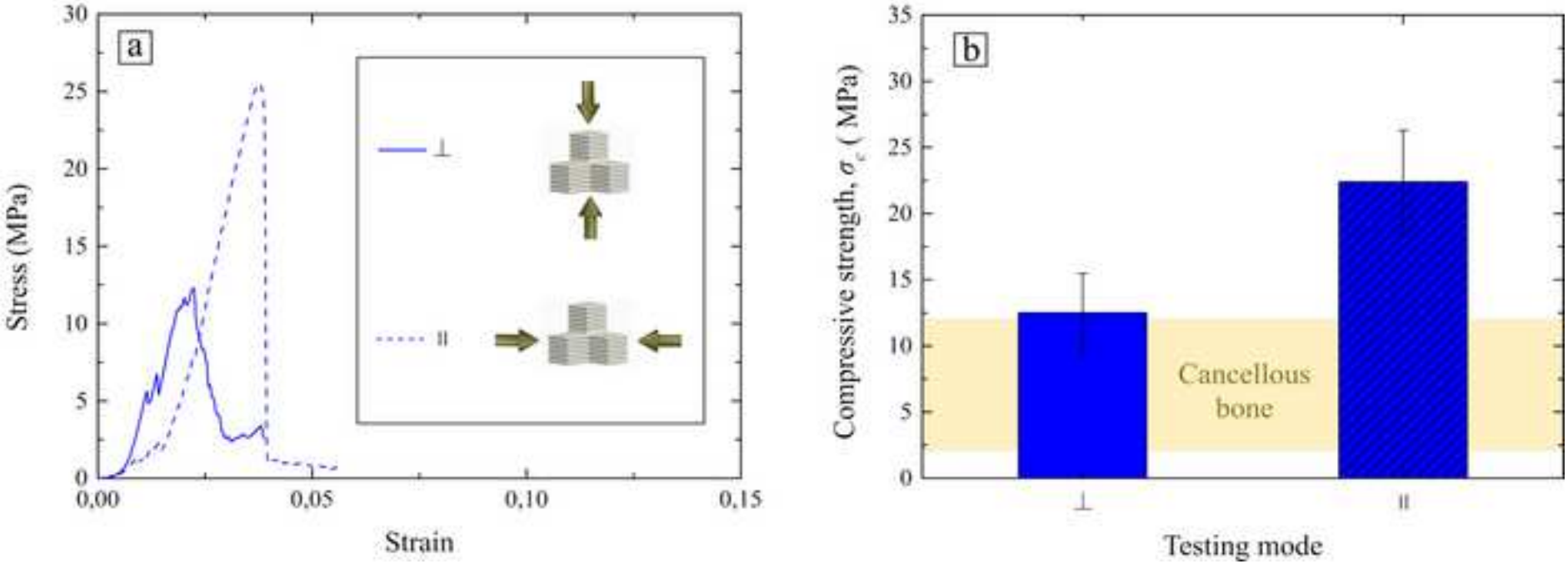

Figure 8

Click here to download high resolution image

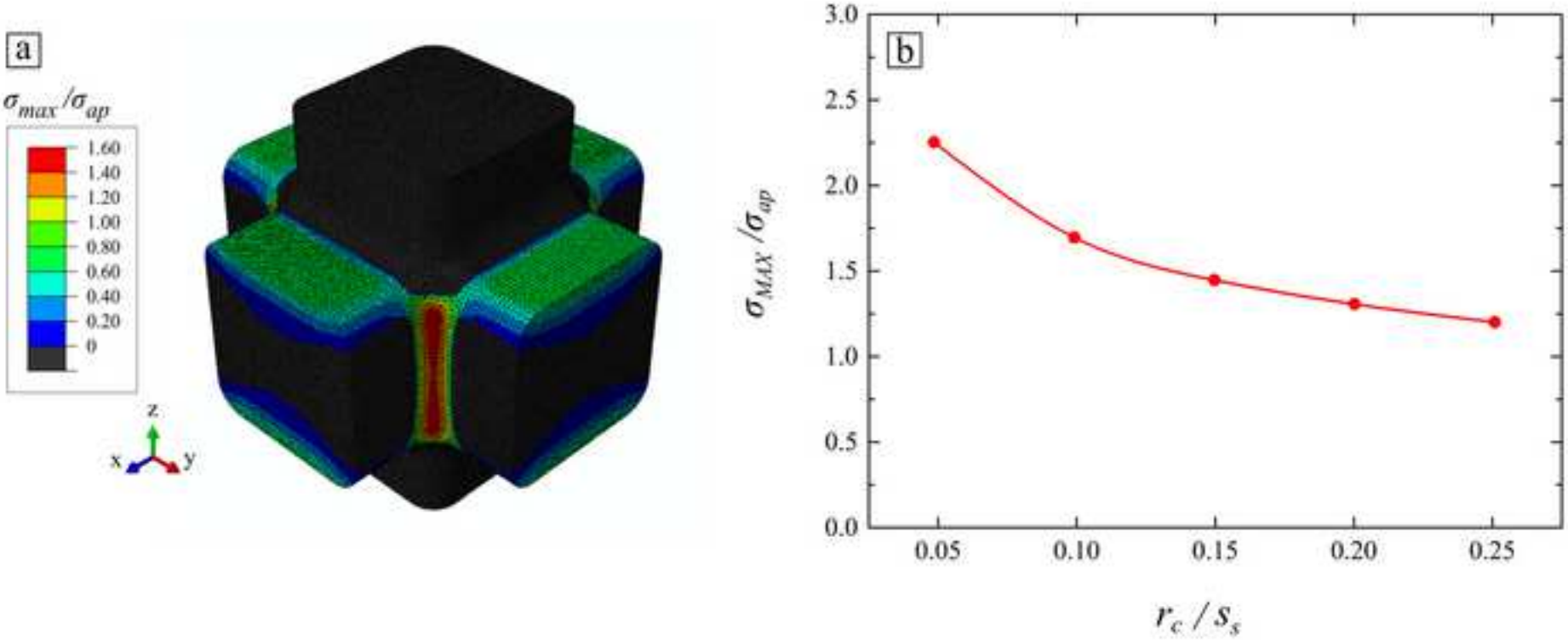

Figure 9

Click here to download high resolution image

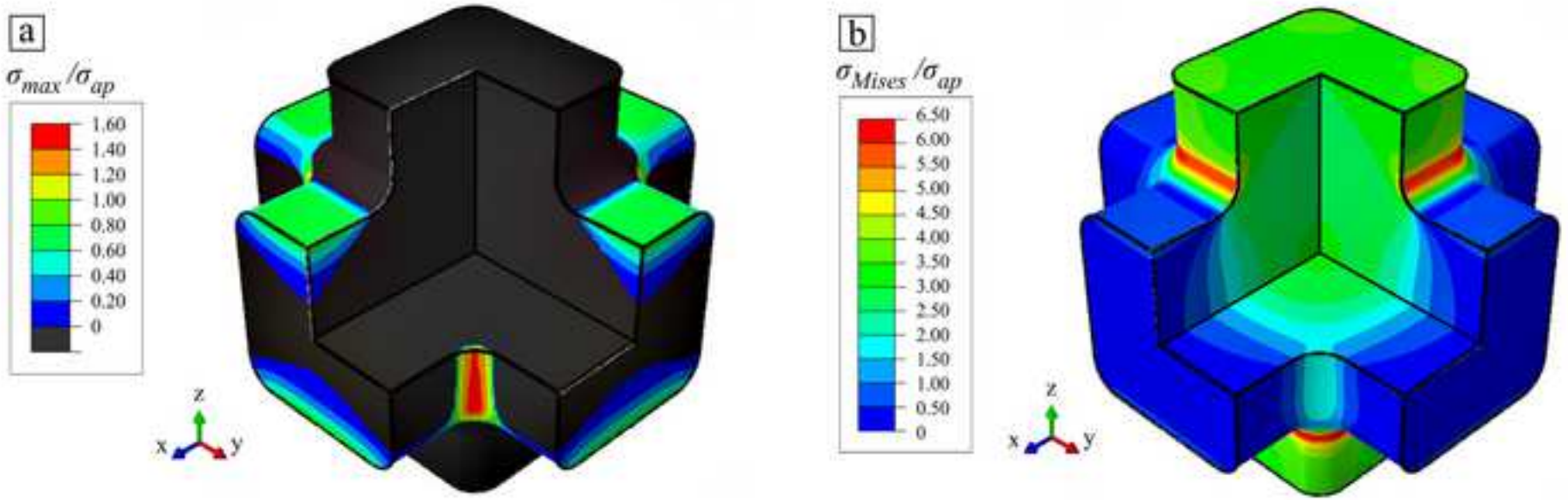

Figure 10

Click here to download high resolution image

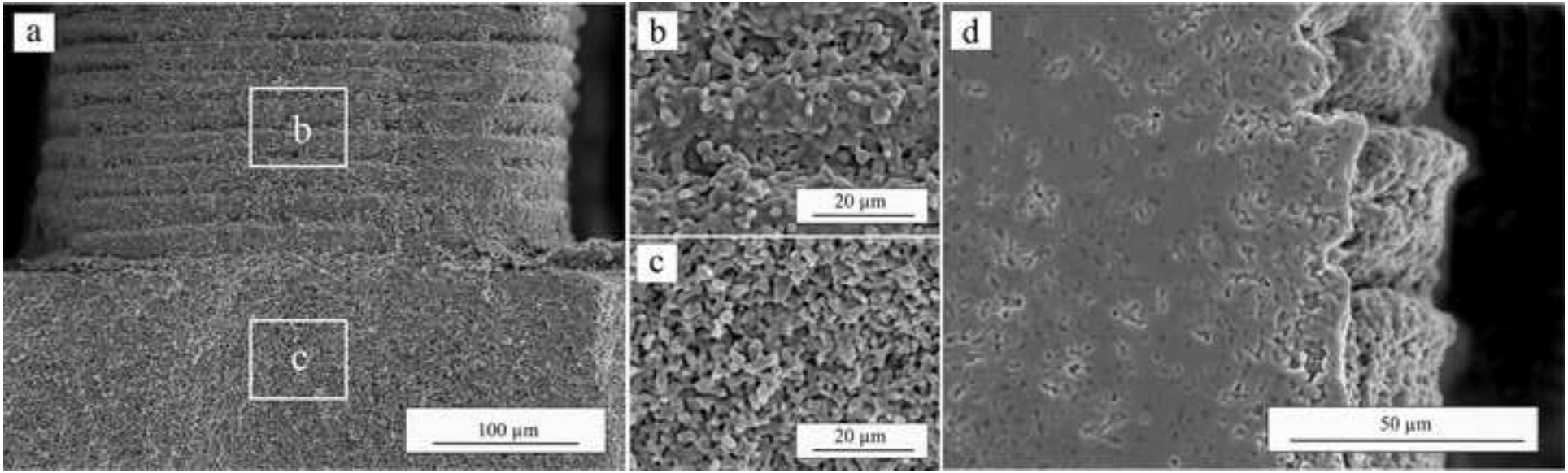

Figure 11

Click here to download high resolution image

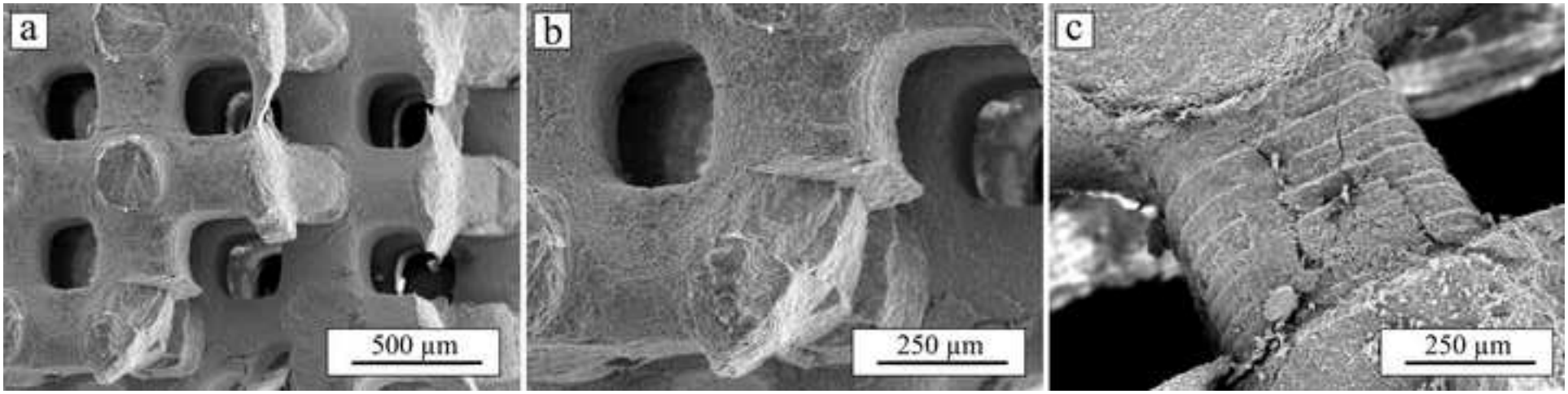

Figure 12

Click here to download high resolution image

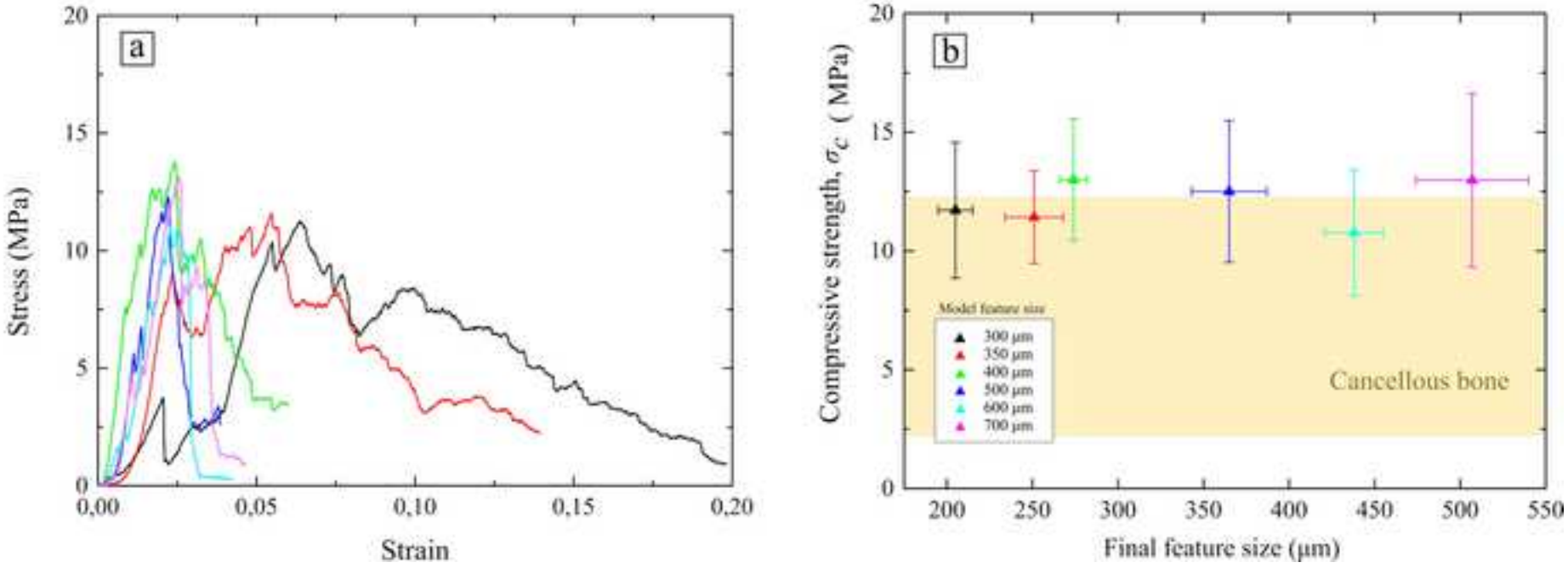

Figure Captions

Figure 1. CAD-models used in this work for the fabrication of the different scaffolds by DLP. Labels indicate their feature (pore and strut) size, which will be used to name each type of structure throughout the manuscript.

Figure 2. Printed scaffold with features size of 500 µm after cleaning and post-printing UV curing.

Figure 3. SEM micrographs of the surface of representative scaffolds with 400 µm model feature dimensions before (a-c) and after (d-f) heat treatment.

Figure 4. Apparent density and total porosity for the fabricated scaffolds after sintering, with indicated model feature dimensions. Data represent mean values with standard deviations as error.

Figure 5. Representative (a) volumetric pore size distribution in a sintered scaffold with 500 µm characteristic size.

Figure 6. SEM micrograph of the transversal midsection of a scaffold with 300 µm feature size. The ceramic material resulting from the densification of the slurry occupying its inner pores can be observed.

Figure 7. (a) Representative stress-strain curves and (b) mean uniaxial compressive strength (with standard deviation as error bar) for scaffolds with 500 µm feature size tested parallel and perpendicular to the printing plane as indicated. The shaded band in (b) represents typical values of human cancellous bone [30], for comparison.

Figure 8. FEM simulation results for scaffolds under compressive loading: (a) Maximum principal stress (normalized by applied stress: $\sigma_{max} / \sigma_{ap}$) contour plot and (b) maximum tensile stress value in the structure (normalized by applied stress: $\sigma_{MAX} / \sigma_{ap}$)

calculated as a function of the radius of curvature at the strut intersections (normalized by strut size: r_c / s_s) in the FEM model.

Figure 9. FEM simulation results for scaffolds under compressive loading: (a) Maximum principal stress, σ_{max}, and (b) von Mises stress, σ_{Mises}, contour plots. Stress values have been normalized by the applied stress, σ_{ap}.

Figure 10. Cross-sectional SEM micrographs of a scaffold fractured perpendicularly to the printing plane (a-c) before and (d) after polishing. Layer grooves are evident at the surface of the struts, but no interlayers defects can be found towards the strut's interior.

Figure 11. SEM micrographs of a fractured scaffold after a uniaxial compression test in the direction perpendicular to the printing plane: (a) Top view showing crack propagation both orthogonal to the printing plane but also diagonally through the vertical struts, with (b) evidence of steps produced by interlayer cracking and (c) hourglass shaped cracks in the transversal orientation, typical of shear driven failure.

Figure 12. (a) Representative load-displacement curves and (b) mean compressive strength as a function of scaffold’s feature size (with standard deviations as error bars), as evaluated in uniaxial compression tests with the load applied perpendicularly to the printing plane. The shaded band represents typical values of human cancellous bone [31], for comparison.

***Declaration of Interest Statement**

Declaration of interests

☒ The authors declare that they have no known competing financial interests or personal relationships that could have appeared to influence the work reported in this paper.

☐The authors declare the following financial interests/personal relationships which may be considered as potential competing interests: